microwave

MDPI

Review

Near-Field Millimeter-Wave FMCW Radar Imaging: A Review of Algorithms and Applications

Dharaben Tandel and Reza K. Amineh *

Department of Electrical and Computer Engineering, New York Institute of Technology, New York, NY 10023, USA; dtandel@nyit.edu

* Correspondence: rkhalaja@nyit.edu; Tel.: +1-347-686-3008

Abstract

Millimeter-wave (mm-wave) near-field imaging using frequency-modulated continuous wave (FMCW) radar has emerged as a pivotal technology for high-resolution applications, including security screening, non-destructive testing, and medical diagnostics. This review evaluates the performance and evolution of key imaging algorithms, categorized into spatial-domain and frequency-domain frameworks. We analyze the delay-and-sum (DAS) beamformer for its real-time utility and the back-projection algorithm (BPA) for its baseline phase precision and robust adaptability to irregular scanning trajectories. To address the high computational demands of standard spatial-domain processing, we examine fast alternatives such as the range migration algorithm (RMA). The exact RMA leverages Fourier-domain operations and Stolt coordinate mapping to achieve optimal computational scaling on uniform grids while preserving diffraction-limited spatial resolutions. Concurrently, we evaluate fast spatial-domain approximations, including Fast Back-Projection (Fast-BPA), which introduces localized Taylor-series expansions to linearize near-field range paths within sub-apertures, accelerating voxel reconstruction times at a reduced computational cost. Furthermore, this study explores advanced modifications designed to overcome physical and operational constraints, such as motion-compensated matched filtering (MF) to eliminate the "stop-and-go" assumption in continuous scanning, and sparse multiple-input multiple-output (MIMO) configurations to mitigate aliasing in undersampled environments. Comparative analysis reveals that while spatial-domain methods (DAS/BPA) generally offer higher robustness to non-uniform aperture perturbations, frequency-domain migration pathways (RMA) maximize the computational throughput required for large-volume three-dimensional (3D) reconstructions. The findings demonstrate that achievable resolution is primarily governed by signal bandwidth and aperture synthesis, though practical performance is often limited by calibration errors and computational overhead. Collectively, these advancements validate the potential of mm-wave FMCW systems to achieve sub-millimeter 3D imaging, bridging the gap between theoretical diffraction limits and real-world indoor sensing challenges.

Keywords: back-projection algorithm; FMCW radar; MM-wave imaging; near-field imaging; range migration algorithm; synthetic aperture radar (SAR)

Check for updates

Academic Editor: Changjun Liu

Received: 15 April 2026
Revised: 6 July 2026
Accepted: 7 July 2026
Published: 13 July 2026

Copyright: © 2026 by the authors. Licensee MDPI, Basel, Switzerland. This article is an open access article distributed under the terms and conditions of the Creative Commons Attribution (CC BY) license.

1. Introduction

Radar imaging has long been recognized as a robust modality for object detection and localization across a wide range of conditions, including low-visibility scenarios [1]. Among various radar architectures, frequency-modulated continuous-wave (FMCW) radar

has gained attention due to its compact implementation, low power consumption, and compatibility with modern complementary metal-oxide-semiconductor (CMOS) technologies [2]. Unlike pulsed radar systems, FMCW radar transmits a frequency-modulated signal commonly referred to as a chirp, enabling simultaneous estimation of range and velocity through analysis of the intermediate frequency (IF) beat signal [3]. These characteristics have led to widespread adoption in automotive sensing [4], industrial monitoring [5], gesture recognition [6], and structural health monitoring applications [7].

A fundamental distinction in radar imaging arises between far-field and near-field operating regimes. In the far-field defined by the Fraunhofer criterion, where the target range R is much larger than $2D^2/\lambda$ (D is the aperture size and λ is the wavelength), the wavefront curvature is negligible, and planar-wave propagation assumptions hold. In contrast, near-field imaging involves targets positioned within the Fresnel zone, where the spherical nature of the wavefront becomes significant and cannot be neglected without introducing substantial phase errors and image defocusing [8]. Millimeter-wave (mm-wave) and sub-terahertz systems used in security or medical testing often operate in the "near-field". At these short distances, the radar waves are spherical rather than flat. To get accurate results, the signal processing technique must be specifically designed to handle this curved geometry [9].

MM-wave FMCW near-field imaging is a critical technology across security, industrial, and medical sectors. In personnel screening, it provides a non-ionizing method for detecting concealed metallic and dielectric threats [10,11]. For non-destructive testing (NDT), it enables the detection of subsurface defects and moisture in composite and dielectric materials [12,13]. In medical imaging, FMCW-based systems have been explored for applications such as breast imaging, where dielectric contrast between healthy and malignant tissues can be exploited [14,15]. These diverse applications share common signal processing challenges, particularly the need for accurate modeling of spherical wave propagation and efficient reconstruction of high-resolution three-dimensional (3D) images.

When reconstructing images from FMCW near-field measurements, the process generally follows one of two paths: the spatial domain or the frequency domain. In the spatial domain, the most straightforward approach is the delay-and-sum (DAS) beamformer, which essentially builds a focused image by coherently summing up the signals reflected to each measurement point [16]. For improved imaging accuracy, the Back-Projection Algorithm (BPA) is widely employed. This method improves imaging accuracy by explicitly computing the exact time-of-flight for each pixel (or voxel) using a spherical wave propagation model [17,18], thereby preserving focusing performance even under non-ideal or irregular radar trajectories [19]. To improve efficiency, frequency-domain methods like the range migration algorithm (RMA), also known as the Omega-K $(\omega - k)$ algorithm, have been proposed that process signals in the wavenumber domain [20]. These techniques rely on Stolt frequency mapping to correct for range cell migration, ensuring that targets remain focused even as their distance from the sensor changes [21,22]. In high-resolution near-field setups, the Omega-K algorithm is often the preferred refinement, as it uses specialized phase-matching filters to handle the complex phase interactions that occur very close to the antenna [13].

Beyond these core methods, matched filtering (MF) is often used to maximize the clarity of the signal against background noise [11]. For 3D imaging, holographic reconstruction methods utilize wave diffraction theory to "back-propagate" the measured field and to reconstruct the target's complex reflectivity [23,24]. Finally, since many modern systems employ multiple-input multiple-output (MIMO) arrays to reduce data acquisition time, co-array signal processing and sparse reconstruction techniques are often adopted to re-

cover missing measurements and suppress aliasing artifacts associated with undersampled apertures [21].

Despite the rapid growth of mm-wave FMCW near-field systems, comprehensive reviews that systematically integrate the underlying signal models, reconstruction algorithms, and application-oriented design considerations remain relatively limited. Existing review articles generally focus on specific reconstruction methods, sensing modalities, or application domains rather than providing a unified perspective across the broader near-field imaging landscape. To establish a transparent and reproducible foundation for this review, the literature was selected using a structured multi-stage methodology. A systematic keyword search was conducted using the IEEE Xplore and Google Scholar databases with Boolean combinations of terms related to short-range radar operation, FMCW systems, millimeter-wave and sub-THz frequencies, and near-field imaging algorithms (e.g., ("near-field" or "short-range") and ("FMCW") and ("imaging algorithm" or "SAR")). The initial search identified approximately 240 candidate publications. These records were subsequently screened according to predefined inclusion and exclusion criteria. Eligible studies were limited to English-language, peer-reviewed journal articles, leading conference proceedings, and official government or organizational publications describing near-field imaging or reconstruction algorithms that account for spherical-wave propagation. Commercial white papers, non-peer-reviewed sources, and studies focusing exclusively on conventional far-field radar processing were excluded. Following this screening process, 44 core publications were selected for detailed analysis and incorporated into the taxonomy presented in this review.

Several review articles have examined related topics from different perspectives. For example, Lopes et al. [25] presented a systematic review of medical microwave imaging with an emphasis on diagnostic performance, repeatability, and biological validation. Xue et al. [26] reviewed fast back-projection algorithms primarily in the context of far-field, spaceborne strip-map SAR imaging. Li et al. [27] surveyed portable short-range microwave sensing systems, focusing on Doppler-based non-contact monitoring, micro-motion sensing, and interferometric target tracking. More recently, Molaei et al. [9] reviewed emerging near-field radar configurations, highlighting security screening systems and deep learning-based imaging approaches. These surveys provide valuable insights into their respective research areas; however, each primarily emphasizes a particular reconstruction methodology or application domain. In contrast, this review adopts a broader system-level perspective by examining the principal near-field imaging algorithms within a unified analytical framework while relating their theoretical foundations to practical system design considerations across multiple application areas.

Specifically, this review establishes a unified observation model that relates spatial-domain DAS beamforming, frequency-domain wavenumber migration techniques, and sub-Nyquist compressed sensing methods within a common analytical framework, thereby enabling a consistent comparison of fundamentally different reconstruction paradigms. The review further examines bistatic imaging configurations and evaluates the phase and localization errors associated with the Phase-Center Approximation (PCA) under ultra-short stand-off conditions, providing practical insights into array design requirements for preserving near-field imaging accuracy and spatial resolution. In addition, the relationships among reconstruction algorithms, hardware architectures, and system-level constraints are systematically analyzed across representative application domains, including security screening, NDT, biomedical imaging, automotive sensing, and gesture recognition. By relating algorithmic characteristics to practical considerations such as computational latency, array aperture, hardware complexity, positioning accuracy, and imaging performance, this review aims to provide a consistent framework for understanding existing techniques and

to offer practical guidance for selecting appropriate imaging algorithms under different operating conditions.

The rest of this review article is organized as follows. Section 2 reviews the fundamental principles and signal model of FMCW radar systems. Section 3 introduces the theoretical foundations of near-field imaging, including wavefront curvature and near-field propagation characteristics. Section 4 presents a unified imaging framework and provides a comprehensive taxonomy and detailed review of six major reconstruction algorithm families: DAS, BPA, $\omega - k$, RMA, multiple-input multiple-output (MIMO), curved synthetic aperture radar (Curved SAR), and compressed sensing (CS). Section 5 compares these algorithms using quantitative performance metrics and computational complexity analyses. Section 6 reviews representative application domains, including security screening, NDT, medical imaging, and short-range target tracking. Section 7 discusses current research challenges and emerging directions, and Section 8 concludes the manuscript.

2. Fundamentals of FMCW Radar

FMCW radar operates by transmitting a "chirp" signal whose frequency increases linearly over time. Unlike traditional pulsed systems, FMCW radars transmit and receive simultaneously, making them ideal for high-resolution, low-power applications. The system identifies a target's position by measuring the time delay τ between the transmitted signal and its reflected echo. Because the transmitter continues to sweep its frequency during the signal's round-trip travel time, the returning echo arrives as a frequency-shifted version of the original. This time delay is defined by the target range R and the speed of light c as [14]:

$$\tau = \frac{2R}{c} \tag{1}$$

By mixing the transmitted and received signals in a mixer known as dechirping, the radar produces a low-frequency intermediate frequency (IF) beat signal. The frequency of this beat f_b is directly proportional to the time delay and the chirp slope α (the rate of frequency increase in Hz/s) [16]:

$$f_b = \alpha\tau = \frac{2\alpha R}{c} \tag{2}$$

This relationship allows a simple Fourier Transform to map spectral peaks directly to target ranges, making the system both computationally efficient and capable of resolving multiple targets simultaneously, as illustrated in Figure 1. The achievable resolution, however, depends on the coordinate domain under consideration. In the range dimension, the range resolution δ_R is determined solely by the transmitted sweep bandwidth B, with:

$$\delta_R = \frac{c}{2B} \tag{3}$$

where larger bandwidths provide finer range discrimination [28]. In contrast, cross-range (azimuth and elevation) resolution is governed by the antenna aperture (D) and wavelength (λ), For conventional real-aperture radar, the angular beamwidth is approximately λ/D, causing lateral resolution to degrade with increasing target distance. The SAR overcomes this limitation by synthesizing a much larger effective aperture through spatial scanning, enabling significantly improved cross-range resolution that can approach the diffraction limit of $\lambda/2$ which is largely independent of range [29]. Doppler or velocity resolution, meanwhile, is determined by the coherent integration interval across multiple chirps, allowing target velocity to be estimated from inter-chirp phase variations.

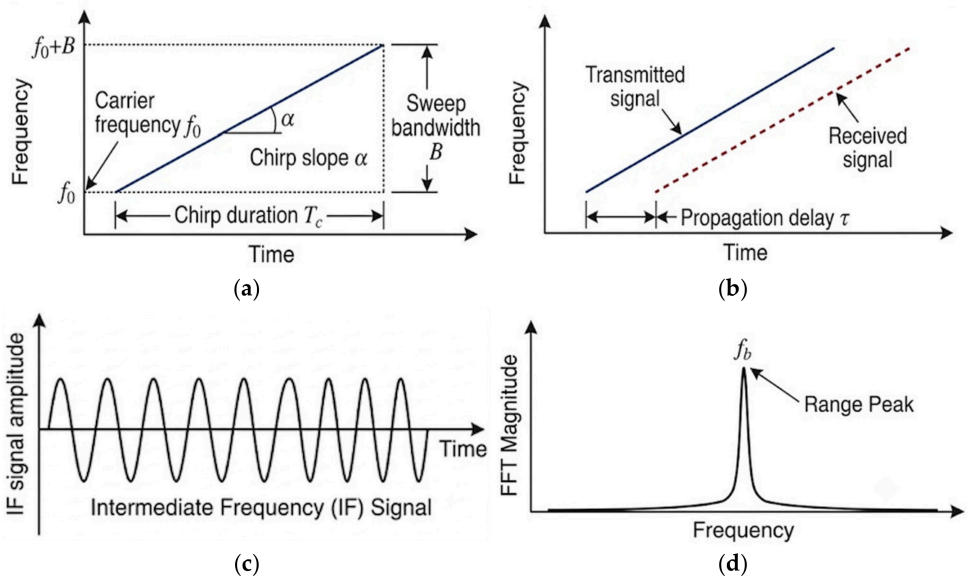


Figure 1. Graphical representation of the FMCW radar signal processing chain: (**a**) a single transmitted chirp illustrating the carrier frequency f_0, sweep bandwidth B, chirp duration T_c, and chirp slope α; (**b**) the time-delayed relationship between transmitted and received signals governed by the round-trip propagation delay τ; (**c**) the resulting intermediate frequency (IF) beat signal in the time domain; and (**d**) the corresponding range spectrum, where a peak at f_b is obtained via the Fast Fourier Transform (FFT).

The accuracy of these measurements also depends on whether the target resides in the far-field or near-field. In the far-field (Fraunhofer zone), which begins at approximately $2D^2/\lambda$, wavefronts are treated as planar, and standard linear phase approximations hold [30]. In contrast, targets located within the near-field (Fresnel region) produce spherical wavefronts whose curvature cannot be neglected. Consequently, the exact propagation distance between the radar and every image point must be modeled to accurately compensate for nonlinear phase variations. These near-field effects are fundamental to high-resolution short-range imaging applications such as medical imaging and NDT, where targets are located within or near the Fresnel region [9,17].

As operating frequencies increase into the mm-wave regime, the wavelength λ decreases, which in turn reduces the Fraunhofer distance. Consequently, targets located at relatively short ranges may still fall within the transition region between near-field and far-field behavior, depending on the aperture size. Accurate imaging in such scenarios requires careful consideration of wavefront curvature and appropriate selection of reconstruction algorithms.

3. Near-Field Imaging Principles

The transition from classical radar theory to near-field imaging requires a fundamental shift in how we model electromagnetic propagation. In the far-field, we often rely on the simplifying assumption that wavefronts arriving at the antenna are planar. However, for short-range FMCW applications where the target lies within the near zone, this approximation collapses. To maintain focus, we must use an exact spherical model. Figure 2 illustrates the geometric configuration of the imaging system. The radar on the aperture plane A located at z_a illuminates a point-wise object at $P(x, y, z)$ on the object plane. This object scatters the waves toward the radar. The imaging algorithm then maps the signal to a corresponding point $P'(x', y', z')$ on the image plane at z' (ideally, we have $(x, y, z) = (x', y', z')$).

For a monostatic radar element at $(x_a,\ y_a,\ 0)$ and a point scatterer at $(x,\ y,\ z)$, the precise two-way travel distance is [24]:

$$R(x_a, y_a) = 2\sqrt{\left\{(x - x_a)^2 + (y - y_a)^2 + z^2\right\}} \tag{4}$$

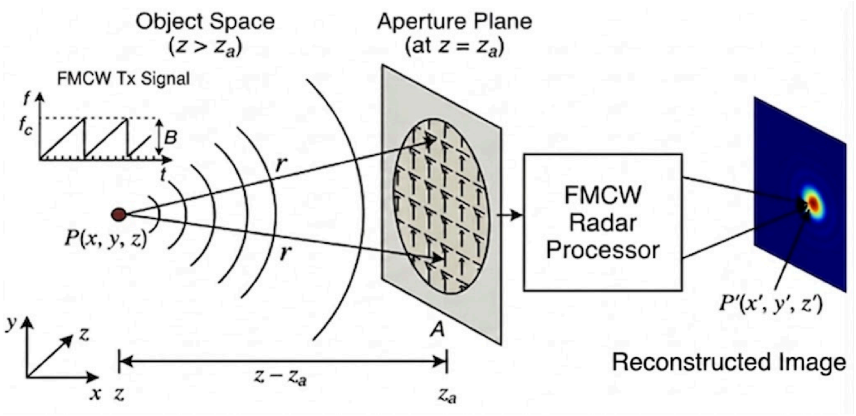


Figure 2. Schematic representation of the FMCW radar imaging system.

When the transmitted chirp with frequency of $f(t) = f_0 + \alpha t$ (f_0 denotes the center or start frequency of the sweep and α represents the chirp rate) reflects off a target, the received beat signal after dechirping encodes this exact distance into a phase term. Unlike far-field models that linearize this relationship, near-field reconstruction preserves the square root form to ensure phase integrity [16]. In the near-field, wavefronts are curved and must be modeled using an exact spherical model. For a monostatic radar element at $(x_a, y_a, 0)$ and a point scatter at (x, y, z), the received beat signal $s(f,\ x_a,\ y_a)$ is expressed as:

$$s(f, x_a, y_a) = \sigma A(f) \cdot \exp\left(\underbrace{-j\frac{4\pi\left(f_0 + \tilde{f}\right)}{c} R(x_a, y_a)}_{\phi(x_a, y_a)}\right) \tag{5}$$

where σ is the complex reflectivity of the target, and $A(f)$ is the frequency-dependent amplitude envelope. The parameter $\tilde{f} \in [0, B]$ represents the frequency shift relative to f_0 over the bandwidth B and $f = f_0 + \tilde{f}$. The received beat signal $s(f, x_a, y_a)$ after dechirping encodes this exact distance into a phase term, $\phi(x_a, y_a)$, which is the argument of the complex exponential in Equation (5).

To turn this raw data into an image, we use a point spread function (PSF) to evaluate how the system responds to a single point. In a back-projection framework, we coherently sum the received signals across all frequencies and aperture positions [16,17]. The resulting image $I(x',\ y',\ z')$ at a candidate point $(x',\ y',\ z')$ is:

$$I(x', y', z') = \iiint s(f, x_a, y_a) \cdot \exp\left(+j\frac{4\pi\left(f_0 + \tilde{f}\right)}{c} R'(x_a, y_a)\right) df\, dx_a\, dy_a \tag{6}$$

where $R'(x_a,\ y_a) = 2\sqrt{(x' - x_a)^2 + (y' - y_a)^2 + z'^2}$ is the hypothesized two-way range to the candidate point, and $s(f,\ x_a,\ y_a)$ is the received beat spectrum.

While the range resolution remains a function of bandwidth $\delta_R = c/2B$, the cross-range resolution in the near-field becomes spatially variant. Because the effective aperture angle changes based on the target's lateral position, the cross-range resolution $\delta_{CR} \approx (\lambda R_0)/L$, where R_0 is the target distance (range), and L represents the physical length of the synthetic aperture. This resolution is no longer uniform across the scene, presenting a unique challenge for consistent imaging [29].

The primary obstacle in this region is the phase error caused by wavefront curvature. If we expand the phase term $\phi(x_a)$ using a Taylor series, we find that the dominant error comes from the quadratic Fresnel phase $\phi_{Fresnel} = -2\pi(x - x_a)^2/\lambda R_0$. If left uncompensated, this term causes significant defocusing [9,21]. In extreme cases where the aperture is electrically large and very close to the target, even higher-order quartic terms become significant, distorting the sidelobes of the image. Because these errors change depending on the target's specific location, a simple "one-size-fits-all" phase correction is impossible [29].

Finally, the shift from far-field SAR to near-field imaging destroys the signal's "separability". In far-field processing, we can often treat range and azimuth as independent variables, which allows for very fast Fourier-based algorithms. In the near-field, these dimensions are inseparably coupled by the spherical range term. To resolve this, advanced frequency-domain methods like the Stolt interpolation or the Omega-K algorithm are used to map the data onto a uniform wavenumber grid. This mapping relies on the dispersion relation [30]:

$$k_z = \sqrt{\left(\frac{4\pi\left(f_0 + \widetilde{f}\right)}{c}\right)^2 - k_x^2 - k_y^2} \tag{7}$$

where k_x and k_y are the cross-range (CR) wavenumbers (corresponding to the x and y aperture directions, respectively) and k_z is the range wavenumber. The image is formed by accurately transforming the data from the $(f,\ k_x, k_y)$ domain to the $(k_x,\ k_y,\ k_z)$ domain. This leads to high-resolution, 3D image reconstructions suitable for critical applications like medical diagnostics or security screening [13,14].

4. Imaging Techniques: Algorithms and Data Acquisition Configurations

Reconstructing a focused 3D image from FMCW radar near-field measurements is fundamentally a challenge of synchronization. The success of the imaging system depends entirely on how effectively the chosen algorithm accounts for the physical antenna layout and the complex, spherical geometry of near-field wave propagation [9,19,29,30]. To provide a clear map of this technical landscape, we have organized the current state-of-the-art techniques into six categories. We begin with the foundational simplicity of the DAS beamformer and progress toward the sophisticated mathematical frameworks of sparse recovery. Each category is characterized by its data acquisition configuration, the antennas, the governing signal model, and the specific adaptations required to resolve near-field effects. The classification framework presented in Table 1 organizes current near-field imaging algorithms into six categories based on two primary criteria: (1) the data acquisition architecture, ranging from mechanically scanned monostatic radars following predefined or random non-planar trajectories to fully static sparse multi-channel arrays; and (2) the processing domain of the image reconstruction algorithm, which performs focusing either through point-by-point time-delay summation in the spatial domain or phase migration over uniformly sampled wavenumber grids.

Table 1. Comprehensive Taxonomy of Near-Field Imaging Techniques.

Category	Antenna Configuration	Algorithm Family	Key Papers	Representative Applications
DAS	Single monostatic; planar/non-planar raster scanning	Coherent DAS; Spherical delay	[14,16]	Medical imaging; Baseline comparison
BPA	Single monostatic; irregular/motion-corrupted trajectories (e.g., handheld or vehicle-mounted)	BPA; Fast-BPA (FFT accel.)	[17,18,28,31]	Automotive SAR; handheld imaging
Omega-K	Single monostatic; uniform planar raster scanning	Holographic RMA; Stolt interpolation	[9,23,24]	Security portals; NDT inspection
MIMO	Sparse $Tx \times Rx$ array; static or short-scan	Virtual aperture; Stolt kernel	[10,32–34]	Fast security screening
Curved	Cylindrical portal;	Cylindrical migration; 3D-BPA	[35]	Circular portals; Structural inspection
Compressed Sensing (CS)	Sub-Nyquist planar; MIMO sparse arrays	ℓ_1-minimization; NIHT; Matrix completion	[36]	High-resolution with reduced scan time

4.1. Unified Signal Model and Notation

At the core of all six algorithm categories lies a single, governing observation equation. While the fundamental physics are established in the planar 2D model in Equation (5), many modern applications involve irregular or non-planar scanning trajectories. To account for these, the observation model is generalized into a 3D format.

For a discrete point scatter at (x, y, z) with a complex reflectivity σ, the beat signal captured at a 3D aperture position (x_a, y_a, z_a) after the dechirping process is expressed as [16,24]:

$$s(f, x_a, y_a, z_a) = \sigma \cdot A(f) \cdot \exp\left(-j\frac{4\pi f}{c} R(x_a, y_a, z_a; x, y, z)\right) \tag{8}$$

In this model, the parameter σ, $A(f)$ and f remain as defined in Section 3. Specifically, $f = f_0 + \tilde{f}$ accounts for the linear frequency-modulated (LFM) waveform sweep, where f_0 is the start frequency and $\tilde{f} \in [0, B]$. $A(f)$ represents the slowly varying amplitude envelope, accounting for antenna gain patterns and path loss.

The critical factor in near-field imaging is the exact two-way range R, defined by the Euclidean distance [30]:

$$R(x_a, y_a, z_a; x, y, z) = 2\sqrt{(x - x_a)^2 + (y - y_a)^2 + (z - z_a)^2} \tag{9}$$

For a standard planar aperture where $z_a = 0$, the Euclidean distance R in Equation (9) represents the spherical wavefront curvature inherent in near-field propagation [29]. To proceed toward imaging, we apply a two-dimensional (2D) spatial Fourier transform over the aperture coordinates $(x_a,\ y_a)$ to derive the angular spectrum [21,24,29]:

$$S(f, k_x, k_y) = \iint s(f, x_a, y_a) \cdot e^{\{-j(k_x x_a + k_y y_a)\}} dx_a dy_a \tag{10}$$

The bridge between these spatial frequencies and the target's depth is the near-field dispersion relation. This identity links the range wavenumber k_z to the CR wavenumbers and the FMCW instantaneous wavenumber $k = 2\pi f/c$ [23,29] as:

$$k_z = \sqrt{4k^2 - k_x^2 - k_y^2} \tag{11}$$

Equation (11) is the foundational identity for near-field wavenumber migration. While far-field models often simplify this by assuming a plane-wave approximation ($k_z \approx 2k$), near-field accuracy depends entirely on retaining the exact square root [11,24]. This precision is what allows the algorithms discussed below to resolve objects located only centimeters from the sensor.

4.2. Category I: DAS Beamforming

4.2.1. Antenna Configuration

DAS beamforming imposes the fewest constraints on antenna geometry. A single monostatic transceiver is physically scanned over a planar or non-planar aperture, and the received beat signal is recorded at each position. Because DAS does not exploit FFT separability, the aperture need not be uniformly sampled. In the reviewed literature, DAS serves as the baseline comparator in biomedical imaging and freehand scanning contexts [14,15,37] and in the comparative study in [16]. Operating frequencies span 24–94 GHz with apertures of 0.3–1 m and standoff distances of 0.1–1 m.

4.2.2. Principle and Near-Field Adaptation

DAS steers a spatial matched filter toward each candidate voxel $(x',\ y',\ z')$ by time-aligning all received waveforms according to the corresponding two-way propagation delay, then coherently summing them [14,16]. In the far-field (Fraunhofer zone), the target is sufficiently distant that the wavefronts arriving at the aperture are effectively planar. Consequently, the phase variations across the aperture become linear, and the delay simplifies to $\tau \approx 2z'/c$, where z' is the axial depth [11]. In the near-field, however, the target resides in the Fresnel zone where the wavefront curvature is pronounced. To maintain focus and prevent phase errors, the exact spherical delay must be retained [16,32]:

$$\tau(x_a, y_a, 0; x', y', z') = \frac{2}{c} R(x_a, y_a, 0; x', y', z') \tag{12}$$

where R is the exact Euclidean distance defined by (9). The range-compressed signal $\widetilde{s}(x_a,\ y_a,\ \tau)$, obtained by inverse FFT (IFFT) of the beat spectrum $S(f, x_a, y_a)$ with respect to the frequency f [32], is evaluated at the per-voxel delay τ defined in Equation (12) via interpolation, and the DAS image is [9,16]:

$$\sigma_{DAS}(x', y', z') = \sum_{x_a} \sum_{y_a} w(x_a, y_a) \cdot \widetilde{s}(x_a, y_a, \tau) \tag{13}$$

where $w(x_a, y_a)$ is an optional aperture taper (e.g., Hamming) applied to reduce sidelobes [28,30]. Equation (13) introduces no approximation to the range term; the near-field spherical geometry is handled exactly through Equation (12) [11,16]. Sheen et al. [30] demonstrated DAS applied to a 35 GHz planar aperture for concealed-weapon detection, and Yang et al. [11] used it for a concealed-object imaging system.

4.2.3. Limitations

The principal limitation of DAS is its resolution. Because aperture weighting in (13) is applied directly to the time-domain waveform, the achievable CR resolution ($\delta_{CR} \approx \lambda R_0/L$). This is spatially variant across the near-field scene [16]. DAS also does not

exploit the full phase history of the FMCW chirp across frequencies to achieve the depth focusing of matched-filter methods [11,24], and its computational cost scales as O(N^5) for a cubic scene identical to standard BPA [17].

4.3. Category II: BPA and Fast-BPA

4.3.1. Antenna Configuration

BPA systems share the single-element monostatic configuration of DAS but extend naturally to irregular, non-planar, or motion-corrupted apertures [16]. The defining property is that the 3D aperture position $(x_a(t),\ y_a(t),\ z_a(t))$ is recorded per pulse from a precision rail, a moving vehicle platform, or an inertial measurement unit (IMU) tracked handheld device [17]. This flexibility is the primary motivation for BPA in automotive SAR and freehand near-field scanning [18,35].

4.3.2. Principle and Near-Field Adaptation

BPA coherently integrates the full beat spectrum over all aperture positions and all FMCW frequencies, applying the exact phase match for each voxel [16,17]:

$$\sigma_{BPA}(x',y',z') = \sum_{x_a}\sum_{y_a}\int s(f,x_a,y_a)\cdot\exp\left(+j\frac{4\pi f}{c}R(x_a,y_a;x',y',z')\right)df \tag{14}$$

In the range-compressed domain, after IFFT over f [16,17]:

$$\sigma_{BPA}(x',y',z') = \sum_{x_a}\sum_{y_a}\tilde{s}(x_a,y_a,R)\exp\left(+j\frac{4\pi f_0}{c}R\right) \tag{15}$$

Here, no paraxial approximation is applied to R, and the exact spherical range in Equation (9) is computed for every aperture-voxel pair. BPA is, therefore, inherently correct in the near-field without any modification [16], a property confirmed experimentally by Xu and Liu [17].

4.3.3. Motion Compensation

Schorlemer et al. [19] modified Equation (15) to compensate for the measured aperture deviations $(\Delta x,\ \Delta y,\ \Delta z)$ from the nominal grid:

$$\sigma_{MC} = \sum_{\{x_a,y_a\}}\tilde{s}\left(\tilde{x}_a,\tilde{y}_a,\tilde{R}\right)\exp\left(+j\frac{4\pi f_0}{c}\tilde{R}\right),\tilde{R} = R(x_a+\Delta x, y_a+\Delta y,\Delta z;x',y',z') \tag{16}$$

Motion-compensated BPA, as described in Equation (16), is capable of fully restoring near-diffraction-limited resolution even when aperture deviation reaches 1.5 mm root mean square (RMS) at 79 GHz. In contrast, the frequency-domain algorithm typically fails under these conditions because the initial aperture FFT step relies on the assumption that data points are collected on an exact, uniform grid [19].

4.3.4. Fast-BPA

Standard BPA has complexity $O(N^5)$ for a cubic volume reconstructed from an N^2 aperture. Xu and Liu [17] reduced this to $O(N^3\log N)$ by decomposing the aperture into P sub-apertures, each containing N/P elements. A local FFT is applied within each sub-aperture to accomplish partial migration, and the resulting sub-images are then coherently

combined to form the final high-resolution reconstruction. Within a specific sub-aperture p, the range is linearized using a first-order Taylor expansion [17,23]:

$$R \approx R_{0,p} + \left.\frac{\partial R}{\partial x_a}\right|_{x_{0,\ p}} \cdot (x_a - x_{0,p}) \tag{17}$$

In this expression, $R_{0,p}$ is the range from the center of the sub-aperture to the target $x_{0,p}$ which represents the phase center (center position) of the p-th sub-aperture, and x_a is the actual position of the radar element within that sub-aperture. Equation (17) introduces a small linearization error per sub-aperture that is negligible when the sub-aperture's half-angle is small [17,23]. The resulting Fast-BPA is validated at W-band (94 GHz) for 3D concealed-object imaging, achieving near-identical image quality to standard BPA at a fraction of the computation time [17].

4.4. Category III: Planar $\omega - k$/RMA

4.4.1. Antenna Configuration

This category is the workhorse of planar near-field FMCW imaging. A single monostatic element is mechanically scanned over a uniform 2D planar grid with step sizes $\Delta x \leq \lambda_{min}/2$ and $\Delta y \leq \lambda_{min}/2$ satisfying the spatial Nyquist criterion [24,30,38]. This configuration is used in security portals, NDT scanners, THz imaging systems, and near-field screening demonstrators [12,13,20,39,40]. Frequencies range from 24 GHz to 340 GHz; apertures span 0.3–1 m; standoff distances range from 0.05 m to 1 m [9,30,39].

4.4.2. Principle: Holographic Phase-Shift Migration

The holographic reconstruction, established by Sheen et al. [30] and adapted to LFM waveforms by Meng et al. [24], applies a depth-dependent phase-shift operator in the wavenumber domain and integrates over frequency to back-propagate the scattered field [23,24,30]:

$$\sigma_{holo}(x', y', z') = \iiint S(f, k_x, k_y) \cdot \exp\left(+j\left(k_x x' + k_y y' + k_z z'\right)\right) df dk_x dk_y \tag{18}$$

where the range of wavenumbers k_z is given by the exact near-field dispersion relation in Equation (11) [23,24,29].

4.4.3. Four-Step RMA Pipeline

i. Aperture FFT: Convert raw data to the angular spectrum $S(f, k_x, k_y)$ using the 2D spatial Fourier transform established in Equation (10) [22,24,30,38].

ii. Matched Filtering: Apply a phase shift at a reference depth z_{ref} using the range wavenumber $k_z(k_x, k_y, k)$, which is functionally dependent on the CR wavenumbers and the instantaneous wavenumber k: [22–24,30]:

$$S_{mf}(f, k_x, k_y) = S(f, k_x, k_y) \cdot exp\left(+jk_z(k_x, k_y, k) z_{ref}\right) \tag{19}$$

iii. Stolt Interpolation: Resample the data to a uniform k_z grid using the dispersion relationship [22–24,30,38]:

$$k = \frac{1}{2}\sqrt{\left\{k_z^2 + k_x^2 + k_y^2\right\}} \tag{20}$$

iv. 3D IFFT: Transform the resampled angular spectrum, denoted as $S_{stolt}(k_x,\ k_y, k_z)$, back into the spatial domain to reconstruct the 3D image [22,24,29,30,38]:

$$\sigma_{RMA}(x', y', z') = IFFT_{3D}\{S_{stolt}(k_x, k_y, k_z)\} \quad (21)$$

4.4.4. Near-Field Adaptation

The near-field property is entirely encoded in (11), the exact square root $\sqrt{(4k^2 - kx^2 - ky^2)}$ replaces the far-field linearization $k_z \approx 2k$ [11,16,24]. Meng et al. [24] further extend (11) to account for LFM waveform imperfections by incorporating the instantaneous chirp wavenumber. Zhang et al. [39] confirmed that at sub-THz frequencies (340 GHz), the exact k_z expression is indispensable for targets within 5 cm of the aperture. Song et al. [28] demonstrated an additional 4–6 dB sidelobe reduction through antenna-pattern compensation applied as a pre-processing weighting of $s(f,\ x_a,\ y_a)$ before the aperture FFT.

4.5. Category IV: MIMO Virtual Aperture and Bistatic RMA

4.5.1. Antenna Configuration

MIMO systems replace the mechanically scanned single element of Categories I-III with a static sparse physical array of Tx transmitters and Rx receivers. Each transmitter-receiver pair $(T_i,\ R_j)$, where $i \in \{1, 2, \ldots,\ T_x\}$ and $j \in \{1, 2, \ldots,\ R_x\}$ synthesizes a virtual phase center at $(x_v,\ y_v)$ [21,29,33]:

$$(x_v, y_v) = \left(\frac{x_{T_i} + x_{R_j}}{2}, \frac{y_{T_i} + y_{R_j}}{2}\right) \quad (22)$$

The $T_x \times R_x$ virtual elements form a large effective aperture without the need for mechanical scanning. Representative systems include the W-band MIMO imager of Shao et al. [33], the NDT system of Bui et al. [12] and Yalcinkaya et al. [13], and the MIMO SAR approach of Yanik and Torlak [21] and Zhuge and Yarovoy [29].

Beyond enabling synthetic voxel reconstruction, this array configuration inherently provides the spatial channels required for digital beamforming and adaptive beam steering. By controlling the phase distribution across the receive array, the radar can electronically steer the main beam and place spatial nulls without mechanical scanning, thereby improving angular selectivity and interference suppression. This capability is particularly important for resolving closely spaced targets with overlapping radar cross-sections. As demonstrated by Singh et al. [41], advanced digital beamforming architectures employing mathematical weighting schemes, such as sum-and-difference beam patterns, can significantly enhance spatial resolution by narrowing the effective radar footprint. Such spatial discrimination is especially valuable in short-range ambient sensing applications, including home-based elderly monitoring, where the radar must simultaneously isolate and track multiple occupants through their spatial locations and micro-Doppler signatures.

4.5.2. Phase-Center Approximation and Near-Field Bistatic Correction

Under the PCA, the bistatic round-trip phase of the pair $(T_i,\ R_j)$ equals twice the monostatic phase at the virtual center in Equation (22). This approximation holds true only when the lateral separation between the i-th transmitter and j-th receiver, denoted by $\left|x_{T_i} - x_{R_j}\right|$ is significantly smaller than the target range R_0 [21,29]. For near-field operation where this condition is violated, Zhuge and Yarovoy [29] derived the exact bistatic Stolt dispersion relation:

$$k_z^{bi} = \frac{1}{2}\left[\sqrt{4k^2 - k_{xT}^2 - k_{yT}^2} + \sqrt{4k^2 - k_{xR}^2 - k_{yR}^2}\right] \quad (23)$$

In this expression, k_{xT}, k_{yT}, and k_{xR}, k_{yR} represent the spatial wavenumbers associated with the transmitter and receiver aperture, respectively. For collocated $T_x \times R_x$ configurations, Equation (23) reduces to the monostatic case in (11) [23,29]. Equation (23) replaces Equation (11) in the Stolt interpolation step (20), giving the MIMO-RMA pipeline: form virtual aperture (22) → 2D FFT (10) → matched filter (19) → bistatic Stolt interpolation (23) → 3D IFFT (21) [21,29]. Yanik and Torlak [21] further applied 2D spatial interpolation on the irregular virtual aperture before the FFT to prevent aliasing from non-uniform virtual element spacing. To preserve mathematical and physical correctness across this pipeline, the cross-range element intervals of the underlying physical array layout must adhere strictly to the spatial Nyquist criterion ($\Delta x \leq \lambda_{min}/2$). Any uncompensated non-uniformity or sparse element dropouts distort the array factor, raising sidelobes within the PSF and introducing spatial aliasing or grating lobes that degrade the dynamic range of both the wavenumber migration and the spatial beamformer.

4.5.3. Near-Field Impact

Bui et al. [12] and Yalcinkaya et al. [13] demonstrate that using the PCA instead of (23) introduces a defect localization error exceeding one range cell $c/2B$ for targets at standoffs below 10 cm with B = 20 GHz, a 7.5 mm error that is unacceptable for structural NDT. Smith & Torlak [22] and Shao et al. [33] utilize the MIMO-RMA kernel in Equation (23) to achieve high-resolution 3D reconstruction from sparse and irregular apertures, outperforming standard PCA-based methods in the near-field.

Similarly, omitting specialized multi-channel phase matching in multi-subject tracking environments leads to target blending, making close-proximity individuals unresolvable. By transitioning from the PCA to rigorous spatial processing frameworks, systems achieve narrow angular resolution boundaries surpassing conventional $\lambda/2D$ limits, which collapse target footprints from several meters down to sub-meter cells. Consequently, utilizing exact phase weighting ensures that spatial multi-channel processing preserves sub-centimeter fidelity and structural isolation, satisfying the stringent performance requirements of both precision structural inspection and smart-home ambient localization [41].

4.6. Category V: Curved and Non-Planar Apertures

4.6.1. Antenna Configuration

This category of techniques deviates from the planar aperture of categories III and IV. Two sub-configurations appear in the literature: (a) cylindrical scanning portals, where the sensor rotates at a fixed radius ρ around the subject [35]; and (b) freehand scanners, where a compact radar is moved arbitrarily with 3D position tracked by IMU [19,32]. Both configurations appear in security screening and structural inspection contexts.

4.6.2. Cylindrical SAR

Gezimati and Singh [35] model the sensor position as $(\rho cos\varphi,\ \rho sin\varphi,\ z_a)$r a one-dimensional (1D) FFT over the axial coordinate z_a, in-plane reconstruction at each axial spatial frequency uses the cylindrical dispersion relation:

$$k_\rho = \sqrt{\left(4k^2 - \frac{k_\varphi^2}{\rho^2} - k_z^2\right)} \tag{24}$$

where k_φ is the azimuthal wavenumber conjugate to φ, and k_ρ is the image radial wavenumber. The 3D image is recovered by a 1D IFFT over k_z after matched filtering in the $(k_\rho,\ k_\varphi)$ plane. Complexity is $O(N^2 \log N)$ per axial slice, lower than the full 3D planar RMA when axial extent is limited [35].

4.6.3. Freehand BPA on Measured Positions

For arbitrary apertures, BPA (14) is applied directly using the IMU-measured 3D positions $(x_a(t),\ y_a(t),\ z_a(t))$ [19,32], so the range becomes:

$$R(t;x',y',z') = \sqrt{\left[(x'-x_a(t))^2 + (y'-y_a(t))^2 + (z'-z_a(t))^2\right]} \tag{25}$$

Álvarez-Narciandi et al. [32] implement this for a freehand 77 GHz scanner and showed that out-of-plane deviations $z_a(t) \neq 0$ are absorbed exactly by (25) without any aperture regularization. The IMU position noise σ_{pos} introduces a phase error $\Delta\varphi \approx (4\pi\sigma_{pos})/\lambda$ at 79 GHz, $\sigma_{pos} = 0.5$ mm gives $\Delta\varphi \approx 1.7$ rad, which remains within acceptable limits for sub-centimeter imaging [19,32].

4.7. Category VI: Compressed Sensing (CS) and Sparse Recovery

4.7.1. Antenna Configuration

This category of imaging systems deliberately undersamples the synthetic aperture to reduce hardware complexity and acquisition time. Common antenna configurations include sparse MIMO arrays, randomly sub-sampled planar raster, or measurement matrices with missing entries [21,32,36]. The defining property is $M \ll N$, where M is the number of available measurements and N is the number of voxels to be recovered [21,36]. To resolve the resulting underdetermined system, these approaches leverage the inherent sparsity of the target scene, where only a few voxels contain significant scattering centers, using reconstruction algorithms such as ℓ_1-minimization or normalized iterative hard thresholding (NIHT) to restore high-resolution 3D images without the grating lobes typically associated with sparse sampling [36].

4.7.2. Measurement Model

To recover the image using sparse reconstruction techniques, the imaging problem is formulated as a linear system. By vectorizing the 3D scene reflectivity into a column vector $\mathbf{x} \in \mathbb{C}^N$, where N is the total number of voxels, and stacking M captured beat-signal samples into a measurement vector $\mathbf{y} \in \mathbb{C}^M$, the near-field forward model is [36]:

$$\mathbf{y} = \mathbf{\Phi x} + \mathbf{n} \tag{26}$$

where $\mathbf{y}$ represents the observed data (the compressed sensing measurements), x represents the unknown target image to be reconstructed, and n represents the additive system noise. The sensing matrix $\mathbf{\Phi} \in \mathbb{C}^{M\times N}$ has its $(m,\ n)$-th element equal to the near-field Green's function response at measurement m due to a unit reflector at the voxel n:

$$\Phi_{\{m,n\}} = \left(\frac{1}{R^2_{\{mn\}}}\right)\cdot\exp\left(-j4\pi k_m R_{\{mn\}}\right) \tag{27}$$

Here, $R_{\{mn\}}$ is the exact two-way range in (9) and $k_m = 2\pi f_m/c$ [32,36]. The near-field spherical amplitude factor $1/R^2$ in (27) is absent from far-field sensing matrices and is essential for near-field reconstruction fidelity.

4.7.3. Recovery Algorithms

When the scene vector x contains at most s-dominant scatterers, it is considered sparse, allowing the use of compressive recovery techniques. The ℓ_1-minimization (LASSO) recovers x from the observation model in Equation (26) [36]:

$$\hat{\mathbf{x}} = \underset{\mathrm{x}}{\operatorname{argmin}} \frac{1}{2}\|\mathbf{y} - \mathbf{\Phi x}\|_2^2 + \lambda\|\mathbf{x}\|_1 \tag{28}$$

In this formulation, the term $\mathbf{\Phi x}$ represents the forward projection of the hypothesized scene into the measurement space, $\|\cdot\|_2$ denotes the ℓ_2-norm (Euclidean distance), $\|\cdot\|_1$ is the ℓ_1-norm used to promote sparsity, and λ is a regularization parameter.

Reissland et al. [36] implemented the NIHT greedy algorithm as a computationally cheaper alternative:

$$\mathbf{x}^{k+1} = \mathcal{H}_s\left[\mathbf{x}^k + \mu\mathbf{\Phi}^{\mathcal{H}}\left(\mathbf{y} - \mathbf{\Phi x}^k\right)\right], \mu = \frac{\|\mathbf{r}\|_2^2}{\left\|\mathbf{\Phi}_{\mathcal{H}_s}\left(\mathbf{\Phi}^{\mathcal{H}}\mathbf{r}\right)\right\|_2^2} \tag{29}$$

where k is the iteration index, $\mathbf{\Phi}^{\mathcal{H}}$ denotes the conjugate transpose (Hermitian) of the sensing matrix, and $\mathcal{H}_s$ is the hard-thresholding operator. The denominator term $\mathbf{\Phi}\mathcal{H}_s$ represents the sensing matrix acting only on the s-largest magnitude components of the back-projected residual, ensuring the step size μ is optimized for the sparse subspace being recovered. The step size is adaptively calculated using the residual vector $\mathbf{r} = \mathbf{y} - \mathbf{\Phi x}^k$. Zhang et al. [32] and Hai et al. [42] complement this with nuclear-norm matrix completion for recovering a full 2D aperture matrix from sparse observations:

$$\hat{\mathbf{S}} = \underset{\mathbf{S}}{\operatorname{argmin}}\|\mathbf{S}\|_* \text{ subjct to}\|\boldsymbol{\mathcal{P}}_\Omega(\mathbf{S}) - \boldsymbol{\mathcal{P}}_\Omega(\mathbf{S}_{\text{obs}})\|_{F\leq\varepsilon} \tag{30}$$

where $\|S\|_*$ denotes the nuclear norm to enforce low-rank structure, $\|\cdot\|_F$ is the Frobenius norm, ε represents the noise tolerance level, and $\mathcal{P}_\Omega$ is the projection operator restricted to the observed indices Ω. The completed matrix $\hat{\mathbf{S}}$ is then processed by the category III RMA pipeline from Equations (19)–(21), combining sub-Nyquist acquisition with FFT-speed focusing.

4.7.4. Near-Field Adaptation

The near-field specificity resides in (27), the exact range (9), and the $1/R^2$ spherical factor ensures $\mathbf{\Phi}$ correctly models near-field propagation [21]. The stronger spatial curvature variation in near-field wavefronts tends to improve the mutual incoherence of $\mathbf{\Phi}$ compared to far-field models, which accelerates convergence of both (28) and (29) [32,36].

5. Performance Metrics and Benchmarking

This section defines key performance metrics applicable to all six categories of techniques and benchmarks each category against those metrics. The computational complexity expressions assume a cubic reconstruction scenario where the $N \times N$ aperture captures N frequency steps to reconstruct an $N \times N \times N$ image volume. The standardization setting where $N_x = N_y = N_f = N$ frequency steps, which allows for a direct "order-of-magnitude" comparison between the different algorithm architectures.

5.1. Performance Metrics

5.1.1. Range Resolution (δ_R)

As defined in Equation (3), range resolution is determined by the FMCW sweep bandwidth B and is common to all six categories of techniques. For instance, for a system

with $B = 4$ GHz, we obtain $\delta_R \approx 37.5$ mm [38] and for $B = 30$ GHz typical of NDT systems, we obtain $\delta_R \approx 5$ mm [13]. Category VI CS can achieve effective range resolution beyond this classical limit, often termed as super-resolution through the sparse recovery framework, contingent on scene sparsity and sufficient SNR [36].

5.1.2. CR Resolution

For a focused planar aperture of extent L, the near-field diffraction-limited cross-range resolution is approximately:

$$\delta_{CR} \approx \frac{\lambda}{2} \tag{31}$$

This is achieved for near-field focused aperture techniques (categories II–V) [21,30]. This limit is spatially invariant for uniform planar apertures such as those used in RMAs (categories III and IV). In contrast, for DAS (category I), CR resolution is spatially variant and approximately $\lambda R_0/L$, causing resolution to degrade with increasing standoff range R_0 [14,16]. For curved apertures (category V), resolution depends on the specific angular extent subtended at the target during the scan [35]. Finally, category VI CS can nominally achieve resolutions better than the diffraction limit of Equation (31) when operating in super-resolution mode, contingent on scene sparsity [36].

5.1.3. Computational Complexity

Table 2 summarizes the time complexity, resolution, and key trade-offs of all six categories of techniques. Standard BPA and DAS share $O(N^5)$ scaling; Fast-BPA and all wavenumber-domain methods achieve $O(N^3 \log N)$; CS scales with the number of iterations and the product MN.

Table 2. Algorithm Performance Comparison Across Six Categories of Techniques.

Category (Cat.)	Time Complexity	Range Resolution	CR Resolution (Focused)	Aperture Requirement	Pros	Cons
Cat. I DAS [14,15,32]	$O(N^5)$	$\frac{c}{2B}$	$\frac{\lambda R_0}{L}$ (spatially variant)	Any geometry	Simplest; no FFT needed; arbitrary aperture	Worst resolution; $O(N^5)$; no phase-history exploitation
Cat. II BPA/Fast-BPA [17–19,28,43]	$O(N^5)$ *std.* $O(N^3 logN)$ *fast*	$\frac{c}{2B}$	$\approx\frac{\lambda}{2}$	Any geometry; irregular	Exact near-field; motion compensation; curved apertures	Standard form is slow; sub-aperture linearization error in Fast-BPA
Cat. III ω-k/RMA [20,21,23,24,29,30,44]	$O(N^3 logN)$	$\frac{c}{2B}$	$\approx\frac{\lambda}{2}$	Uniform planar grid	Optimal computational scaling on uniform grids; exact k_z dispersion; well-established	Planar grid only; Stolt interpolation error if undersampled
Cat. IV MIMO + RMA [10,22,29,31–34]	$\approx O(N^3 logN)$	$\frac{c}{2B}$	$\approx\frac{\lambda}{2D_v}$	Regular virtual grid; bistatic correction near-field	Large aperture from a few elements; no mechanical scan	PCA error at close range; tight $TX \times RX$ synchronization required

Table 2. *Cont.*

Category (Cat.)	Time Complexity	Range Resolution	CR Resolution (Focused)	Aperture Requirement	Pros	Cons
Cat. V Curved SAR [32,35]	$O(N^2 log N)$ *slice* *or* $O(N^5)$ *BPA*	$\frac{c}{2B}$	Geometry-dependent	Cylindrical or freehand (requires IMU)/optical position data	Handles portals and handheld; exact for curved geometry	IMU accuracy critical; no standard FFT pipeline
Cat. VI CS/Sparse [32,36,42]	$O(\text{iter}\cdot M\cdot N)$	$\leq \frac{c}{2B}$	$\leq \frac{\lambda}{2}$ (sparsity dependent)	Sub-Nyquist; sparse or random	Sub-Nyquist sampling; super-resolution potential	Slow for large N; sparse scene required; SNR threshold

5.1.4. PSF and Sidelobe Level

All matched-filter algorithms (Categories II-V) yield the same theoretical PSF width given by Equations (3) and (31) [30,38]. With a rectangular aperture, the sidelobe level is −13 dB for all methods due to the inherent properties of the *sinc*-function. Applying a Hamming taper reduces sidelobes to approximately −42 dB at the cost of a 25–50% main-lobe broadening [38]. DAS (Category I) exhibits worse sidelobe performance than matched-filter methods because it does not coherently combine the full phase history over the frequency-aperture grid [16]. Finally, Song et al. [28] demonstrate an additional 4–6 dB sidelobe reduction through antenna-pattern compensation applied directly within the Category III pipeline.

5.1.5. SNR and Coherent Integration Gain

Matched-filter methods (Categories II-V) achieve a coherent integration gain of $G = 10\log_{10}\left(N_x N_y N_f\right)$ dB over single-element reception by coherently processing the full 3D phase-history volume [30,38]. In contrast, DAS achieves a spatial gain of $G = 10\cdot\log_{10}(N_x N_y)$dB as it does not typically exploit the same degree of coherent frequency integration as migration-based techniques [16]. Lastly, Category VI CS requires the scene SNR to remain above a threshold dictated by the sensing matrix's mutual coherence and sparsity level of the target; below this critical threshold, the recovery fails sharply, leading to significant image artifacts [32,36].

5.2. Category-by-Category Benchmarking

5.2.1. Category I (DAS)

DAS represents a structurally straightforward approach but provides lower comparative resolution performance. Its $O(N^5)$ cost equals standard BPA, and its cross-range resolution of $\lambda R_0/L$ is spatially variant and worse than the near-field diffraction limit $\lambda/2$ achievable by categories II-V [16]. DAS does not exploit FMCW phase coherence across frequencies; it is therefore used primarily as a baseline comparator and in systems where implementation simplicity outweighs image quality, such as the real-time concealed-object system of Liu et al. [10].

5.2.2. Category II (BPA/Fast-BPA)

BPA serves as a primary reference standard for non-uniform, irregular, or motion-corrupted trajectories, as it directly incorporates measures of out-of-plane positional derivations $(\Delta x,\ \Delta y, \Delta z)$ into the per-voxel distance calculations. While standard BPA is $O(N^5)$ prohibitive for large 3D volumes, Fast-BPA reduces this to $O(N^3 \log N)$ [17]. The unique strength of BPA is its inherent capacity for motion compensation. In Equation

(16), Schorlemer et al. [19] demonstrated full resolution recovery after 1.5 mm RMS aperture deviations at 79 GHz, whereas category III frequency-domain methods fail under the same deviations. Consequently, BPA is highly advantageous for handling freehand apertures and automotive SAR platforms without requiring an additional aperture regularization step.

5.2.3. Category III (Planar ω-k/Holographic RMA)

Category III exhibits optimal computational scaling $O(N^3 \log N)$ among exact reconstruction approaches, running significantly faster than standard back-projection routines for equivalent scene dimensions. Amineh [16] confirms it is 3 to 10 times faster than BPA for equivalent scene sizes. However, the Stolt interpolation in Equation (20) can introduce spectral leakage if the resampled k_z grid is undersampled. In practice, 2 to 4 times oversampling of the Stolt grid is recommended to maintain fidelity [30,38]. The critical limitation remains the requirement for a uniform planar aperture, as any deviation corrupts the 2D aperture FFT in Step 1 [38].

5.2.4. Category IV (MIMO Virtual Aperture RMA)

MIMO achieves large effective apertures at reduced hardware cost. The bistatic correction in Equation (23) is essential for targets at standoff below 10 cm at mm-wave frequencies to avoid geometric distortion [12,13]. Zhuge and Yarovoy [29] showed that omitting the bistatic phase correction and instead relying on the PCA in Equation (23) degrades cross-range resolution by 30–50% for near-field targets. Conversely, applying the exact bistatic Stolt dispersion relation in Equation (23) allows the system to recover the full diffraction-limited resolution of $\lambda/2$ [34].

5.2.5. Category V (Curved/Non-Planar SAR)

Cylindrical SAR frameworks, as defined in Equation (24), have complexity of $O(N^2 \log N)$ per axial slice, which is computationally lower than the full 3D planar RMA when axial extent is limited [35]. The binding constraint for such non-planar geometries remains the IMU accuracy: the position must satisfy $\sigma_{pos} < \lambda/4\pi$ to keep the residual phase error below 1 rad. At 79 GHz this necessitates a $\sigma_{pos} < 0.48$ mm which is a threshold achievable with high-grade tactical IMUs or optical tracking systems [19].

5.2.6. Category (VI–CS/Sparse Recovery)

CS provides a path for sub-Nyquist acquisition and potential super-resolution. However, the computational cost is high; the NIHT iteration in Equation (29) costs $O(MN)$ per iteration, often requiring 50–500 iterations and $M \approx 0.4N^3$, which far exceeds $O(N^3 \log N)$ cost of category III for large voxel volumes [36]. Reissland et al. [36] showed that for a sparse scene ($s \leq 0.1N$ non-zero voxels), CS can recover from 40% of the Nyquist measurements at approximately 20 times the computation time of standard RMA. Consequently, this approach is best suited for scenarios where the scene exhibits true spatial sparsity (e.g., isolated internal composite cracks or buried metallic elements) rather than continuous, distributed target geometries [36,38].

6. Applications

The six categories of techniques identified in Section 4 are deployed across five application domains. Table 3 maps each domain to the relevant categories, the associated antenna configuration, the key near-field engineering challenges, and the relevant references.

Table 3. Application Domain vs. Technique Category Mapping.

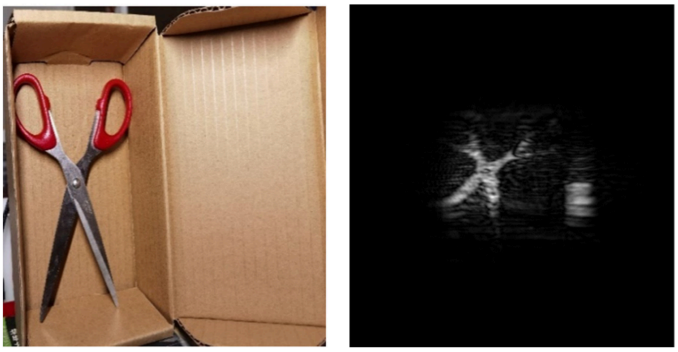
Application Domain	Algorithm Categories	Antenna Configuration	Key Near-Field Challenges	Key References
Security Screening & Personnel Imaging	Cat. I (DAS baseline), II (BPA freehand), III (ω-k portal), IV (MIMO fast-scan), V (cylindrical)	2-D planar raster (portal); cylindrical scanner; handheld IMU-tracked wand	Real-time throughput; non-cooperative subjects; standoff 0.3–1 m; dielectric threat detection	[9,10,18,24,30,38]
Non-Destructive Testing (NDT)	Cat. III (ω-k/THz), IV (MIMO bistatic RMA), VI (CS sparse defects)	Planar monostatic raster or MIMO sparse array; standoff 1–10 cm	Sub-mm defect resolution; B up to 30 GHz; material penetration; defect localization accuracy	[12,13,20,39,40,42]
Medical Imaging	Cat. III (holographic), IV (MIMO + bistatic RMA)	Conformal or planar MIMO array; near-body standoff 5–20 cm	Heterogeneous dielectric tissue; effective wavenumber $k_{eff} = 2\pi f\sqrt{\varepsilon_r}/c$; motion artifacts	[14,15]
Automotive & Short-Range SAR	Cat. II (BPA + motion comp.), III (ω-k straight aperture)	Single FMCW transceiver on moving vehicle; synthetic aperture from platform motion	Platform motion compensation; near-field at $R < 5$ m; real-time constraint at 77 GHz	[19,44]
Gesture & Hand Recognition	Cat. III (ω-k/SAR sequential frames)	Compact fixed-aperture FMCW radar at 77 GHz	Dynamic target; limited aperture; real-time frame rate 10–30 Hz; near-field at 0.1–0.3 m	[31]

6.1. Security Screening and Personnel Imaging

Personnel screening for concealed weapon detection is the most extensively studied application in the reviewed literature and spans all five primary imaging algorithm categories. The foundational category III holographic system of Sheen et al. [30] utilizes a 35 GHz monostatic raster scanner with the four-step RMA pipeline from Equations (18)–(21) to achieve sub-centimeter 3D resolution at 0.3 m -1 m standoff, a level of precision sufficient to detect both metallic and dielectric threats. Haegelen et al. [18] implemented a comparable near-field SAR scanner at millimeter-wave frequencies and confirmed that utilizing the exact k_z dispersion relation of (11) is a mathematical requirement for accurate focusing when the target is within 0.5 m of the aperture.

For high-throughput applications, MIMO-based screening (category IV) has become a preferred architecture. Yanik and Torlak [21] demonstrated that sparse MIMO arrays using bistatic RMA in Equation (23) can achieve image quality equivalent to single-element raster scans while drastically reducing mechanical acquisition time. The bistatic phase correction in (23) is particularly critical at portal standoffs below 0.5 m, where the phase-center approximation fails. Furthermore, Yang et al. [11] and Peng et al. [43] confirm that near-field 3D SAR processing with the exact dispersion relation is essential for accurate concealed-item localization within the geometric constraints of a security portal.

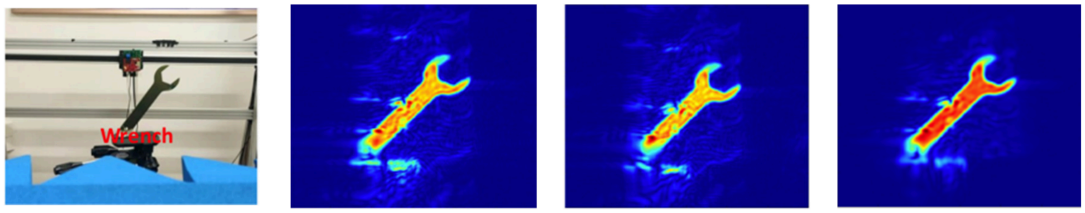
Beyond high-fidelity reconstruction, recent research emphasizes the integration of imaging with automated classification. Liu et al. [10] proposed a concealed object detection and recognition system using a 120 GHz FMCW radar, demonstrating that even with the simplified hardware constraints of a compact scanner, high-frequency mm-wave data can be leveraged for the automated recognition of hazardous items, as shown in Figure 3. Their work underscores that for practical security applications, the imaging algorithm (category III) must be coupled with robust feature extraction to minimize human intervention.



(**a**) (**b**)

Figure 3. (**a**) Actual picture of scissors covered by a paper box; (**b**) SAR image of scissors covered by a paper box 90 mm away from the radar [10].

Finally, recent efforts have focused on enhancing the fidelity of spatial-domain methods. In an experimental darkroom setup evaluating a wrench model at a distance of $z_0 = 300$ mm, Song et al. [28] et al. demonstrated 2-D SAR reconstruction using an approximate virtual array spanning ± 150 mm across both the x and y axes. While maintaining a horizontal sampling interval of 0.5 mm, the authors noted that configuring the vertical antenna sampling interval to exceed half a wavelength by 2 mm introduced artifacts, specifically resulting in a ghost image within the final reconstruction. Furthermore, a rigorous comparison between RMA, standard BPA, and an Enhanced BPA (category II). They demonstrate that their enhanced BPA, which incorporates antenna-pattern compensation, suppresses sidelobe artifacts caused by non-uniform antenna gain, improving target contrast by 4–6 dB and outperforming standard category III implementations in ultra-near-field scenarios, as illustrated in Figure 4.



(**a**) (**b**) (**c**) (**d**)

Figure 4. (**a**) Optical image of a wrench, (**b**–**d**): Reconstructed 2D SAR images over a 150 mm × 150 mm field of view (horizontal x-axis and vertical y-axis): (**b**) 2D wrench imaging result in BPA, (**c**) 2D wrench imaging result in RMA with amplitude loss compensation, (**d**) 2D wrench imaging result in Enhanced BPA [28].

6.2. NDT and Structural Inspection

NDT demands the highest resolution within the reviewed application space, because targets are sub-millimeter defects such as delamination, voids and surface cracks embedded in dielectric materials. Standoff distances are typically 1–10 cm and sweep bandwidths of 20–30 GHz are required to achieve the sub-5 mm range resolution needed for structural integrity assessment [12,13].

Category III (holographic/RMA imaging) is the baseline NDT method. Zhang et al. [39] applied the full RMA pipeline (18)–(21) at 340 GHz to detect delamination in ceramic composites, demonstrating that the exact k_z expression in (11) is indispensable for targets within 2 cm of the aperture. Qian et al. [40] presented a near-field THz SAR system for NDT and confirmed that depth-of-defect estimation requires the near-field dispersion relation rather than the far-field approximation.

For production-line NDT where high-speed acquisition is critical, category IV systems (MIMO with bistatic RMA) are preferred as they eliminate the need for mechanical scanning. However, operating at close proximity to a target requires high-fidelity signal modeling to avoid geometric distortion. Bui et al. [12] and Yalcinkaya et al. [13] demonstrated that relying on the standard PCA, which assumes the bistatic pair acts as a single monostatic element and introduces significant localization errors for targets at standoffs below 10 cm. At sweep bandwidth $B = 20$ GHz, this approximation results in a displacement error exceeding 7.5 mm (one range cell), a margin that is unacceptable for precision structural NDT. To resolve this, Zhuge and Yarovoy [29] confirmed that utilizing the full bistatic near-field kernel in (23) compensates for these geometric phase errors. This advanced modeling maintains diffraction-limited 3D resolution even at a 5 cm standoff.

Category VI (CS) is particularly well-suited to NDT because defect sites are genuinely sparse within a largely transparent background material, satisfying the sparsity assumption required for recovery in (28). Reissland et al. [36] showed that NIHT recovery (29) from 40% of the Nyquist aperture samples localizes near-field targets with accuracy equivalent to full-aperture BPA at significantly reduced scan time.

6.3. Medical Imaging

Medical mm-wave FMCW imaging is motivated primarily by breast cancer detection, where malignant tissue exhibits measurably higher dielectric contrast than healthy tissue at mm-wave frequencies [14,15]. The key near-field challenge unique to this domain is heterogeneous dielectric propagation, as electromagnetic waves traversing complex biological tissues experience reduced propagation velocity and depth-dependent attenuation governed by the local complex relative permittivity, $\epsilon^* = \epsilon' - j\epsilon''$ [15]. Accordingly, the effective wavenumber within biological tissue is expressed as $k_{eff} = 2\pi f\sqrt{\varepsilon_r}/c$, where ε_r denotes the local relative permittivity of the tissue. Instead of using the free-space wavenumber defined in (11), practical imaging systems employ either an effective homogeneous approximation or a layered dielectric model to compute the propagation constant. The corresponding near-field dispersion relation, $k_z = \sqrt{4k_{eff}^2 - k_x^2 - k_y^2}$ is then used to compensate for wavefront refraction and phase accumulation within heterogeneous tissue. Inaccurate estimation of spatial dielectric distribution introduces phase errors that manifest as image defocusing, geometric distortion, and depth localization inaccuracies. [14,15].

Beyond propagation effects, clinical implementation imposes stringent hardware and signal processing requirements. The strong reflection generated at the air-skin interface often masks the comparatively weak backscattered signals originating from subsurface tumors, necessitating advanced clutter suppression and multi-static signal subtraction techniques during preprocessing [15]. In addition, physiological motion, including respiration and involuntary patient movement, can introduce significant phase instability and image degradation. Consequently, practical systems require rapid data acquisition while maintaining compliance with non-ionizing electromagnetic exposure limits.

Maier et al. [14] evaluated an FMCW radar system against a VNA-based reference platform operating over a 6–14 GHz bandwidth, which provides a range resolution of approximately 1 cm in fat tissue. While the hardware utilizes a multi-antenna configuration, the reconstruction is performed using the DAS algorithm (category I). Their results demonstrate that the FMCW-DAS approach matches VNA-DAS image quality and dynamic range while achieving a tenfold (10×) reduction in acquisition time. This confirms that for clinical diagnostics, high-speed FMCW sweeps can match laboratory-grade fidelity at significantly lower costs [14].

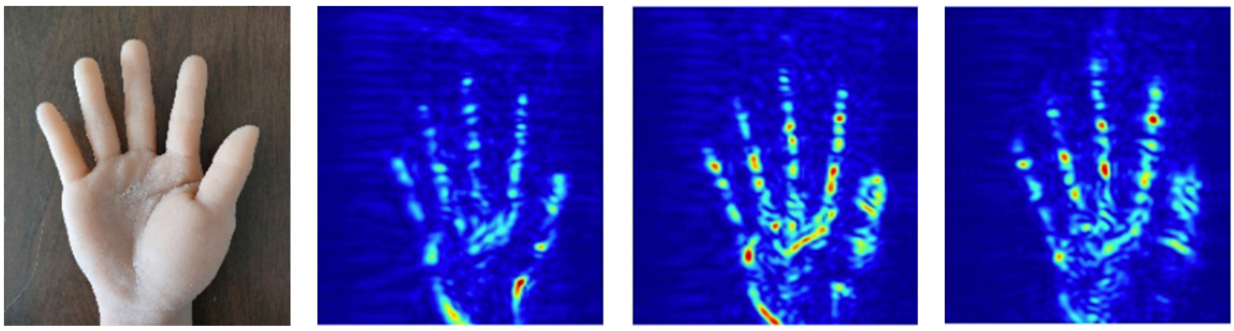
6.4. Automotive and Short-Range SAR

Automotive systems exploit the vehicle's own motion to synthesize a large SAR aperture using compact 77 GHz FMCW transceivers. S.N.T.S et al. [44] applied the category III ($\omega - k$/RMA) algorithm to automotive SAR data, demonstrating that wavefront curvature is significant for targets at ranges $R < 5$ m, requiring exact near-field focusing. Similarly, Hao et al. [31] used near-field FMCW-SAR for hand gesture recognition, where the exact dispersion relation (11) is required for resolving fine motor features at ultra-short ranges of 0.1–0.3 m.

Category II (BPA with motion compensation) is traditionally favored for automotive scenarios due to its ability to handle the inherently irregular platform motion encountered on real roads [44]. However, when a sufficient linear trajectory can be maintained, category III is preferred for its $O(N^3 \log N)$ computational efficiency. To maintain focus in these frequency-domain methods, Schorlemer et al. [19] demonstrated that GPS/IMU-derived motion data must be applied as a phase pre-correction to the raw signal $s(f, x_a, y_a)$ before the initial aperture FFT. This compensation is critical; at 79 GHz, even sub-millimeter position jitter can corrupt the phase history, a challenge Schorlemer addresses through rigorous motion-compensated signal modeling.

6.5. Gesture and Hand-Motion Recognition

Hao et al. [31] demonstrated near-field FMCW-SAR imaging applied to static hand gesture recognition at 77 GHz. A fixed-aperture compact radar applies the category III ($\omega - k$) pipeline (18)–(21) to produce sequential 2D SAR images of the hand at video-like frame rates. The near-field condition is inherent: at 0.1 m −0.3 m standoff with a 10 cm aperture, the Fraunhofer distance $2D^2/\lambda$ is approximately 5 m. Thus, the exact dispersion relation in (11) is required for accurate shape reconstruction [11,31]. Notably, Hao et al. [31] observed that imaging results vary significantly with distance; in their experimental configuration, optimal imaging quality was achieved at a standoff distance (the range between the radar and the hand) of 380 mm, with a slight degradation in resolution and contrast observed at closer (360 mm) or farther (400 mm) distances, as shown in Figure 5.



(**a**) (**b**) (**c**) (**d**)

Figure 5. Static gesture imaging results in an unobstructed scene (**a**) Gesture five and its image at standoff distances of (**b**) 360 mm, (**c**) 380 mm, and (**d**) 400 mm [31]. The exact numeric values and labels for the images' axes have not been provided in the original work.

For applications operating at real-time frame rates of 10–30 Hz, Category III algorithms are generally considered the most practical among the reconstruction methods reviewed. At the typical scene sizes used for hand tracking ($N \approx 64$ per dimension), the $O(N^3 \log N)$ cost of $\omega - k$ algorithm is compatible with real-time GPU implementation [23,31], whereas BPA at $O(N^5)$ and category VI (CS) are computationally too expensive for high-frame-rate

operation without employing significant approximations that would compromise the fine spatial resolution required for gesture differentiation [36].

6.6. Cross-Domain Design Guidelines

The domain analyses establish a consistent framework for algorithm selection based on specific operational constraints. In security screening, the choice is dictated by the physical scanner architecture: category III remains the baseline for precision planar portals [18,30] while category IV (MIMO) is utilized to maximize throughput via electronic scanning [21]. For irregular geometries, category II (BPA) and category V (Cylindrical) are essential for handheld or 360-degree scanners, respectively [32,35] with category I (DAS) reserved for real-time applications where hardware simplicity is paramount [10].

In NDT, where sub-millimeter precision is required, categories III and IV dominate due to their exact wavenumber kernels [12,13,39], while category VI (CS) offers a unique advantage for localizing sparse internal defects with sub-Nyquist data [36]. In medical imaging, current research demonstrates that category I (DAS) can match laboratory-grade VNA fidelity at 6–14 GHz, provided it is optimized for high-speed FMCW acquisition [14], though Category IV (MIMO-RMA) is theoretically superior for scaling to 3D clinical volumes [29].

For automotive SAR, the trade-off is between geometry and speed: category II is required to compensate for irregular motion and sub-millimeter phase jitter [19], while category III is preferred for computationally efficient processing of linear trajectories [23,44]. Finally, in gesture recognition, the extreme constraints of 10–30 Hz frame rates and ultra-short-range focusing make category III the only viable algorithmic option for maintaining real-time interaction [31]. These guidelines provide a systematic framework for future FMCW near-field imaging system developments [9,28].

7. Open Research Challenges and Future Directions

Despite significant progress in near-field mm-wave FMCW imaging algorithms, several open challenges remain in enabling a reliable transition from controlled experimental setups to real-world operational environments. These challenges span computational scalability, array calibration, material-dependent propagation effects, and multi-channel synchronization issues.

7.1. Real-Time Computational Scaling of Spatial-Domain Reconstructions

Frequency-domain migration techniques such as the RMA generally exhibit favorable computational efficiency, typically in the order of $O(N^3 \log N)$, but their applicability is largely restricted to uniform planar geometries. In contrast, spatial-domain methods such as the BPA provide greater flexibility, as they directly incorporate exact Euclidean distance calculations for arbitrary and non-ideal trajectories, including motion-corrupted acquisitions. However, conventional BPA implementations exhibit high computational complexity, approximately $O(N^5)$, which can limit their scalability for large-scale 3D reconstructions.

Fast back-projection variants reduce this computational burden to approximately $O(N^3 \log N)$ through localized approximations and sub-aperture formulations, although such approximations may introduce phase errors in ultra-near-field conditions where high precision is required. Accordingly, efficient implementation strategies based on parallel computing architectures, particularly GPU acceleration, remain an active area of research. In addition, extensions of non-uniform fast Fourier transform (NUFFT)-based methods capable of handling irregular spatial sampling without explicit point-by-point delay calculations represent a promising direction.

7.2. Mutual Coherence and Computational Overhead in Compressed Sensing

Compressed sensing and sparse recovery frameworks provide an effective approach for reducing data acquisition requirements and alleviating mechanical scanning constraints through sub-Nyquist sampling strategies. However, the performance of such methods is strongly dependent on the coherence properties of the sensing matrix, which becomes increasingly challenging in near-field scenarios due to spherical wave propagation effects and distance-dependent amplitude decay.

The resulting sensing matrices typically scale with voxel density, leading to significant computational demands in iterative reconstruction methods such as ℓ_1-minimization and NIHT. In large-scale or less-sparse scenes, the associated computational cost, which scales with the number of iterations and matrix dimensions, may become substantial.

To address these limitations, learning-based reconstruction approaches, including unrolled optimization networks such as learned iterative shrinkage-thresholding algorithms, have been explored. These methods aim to reduce iterative complexity by learning compact representations of the inverse scattering process while maintaining reconstruction accuracy.

7.3. Array Calibration and Inter-Channel Synchronization in Near-Field MIMO Systems

MIMO array configurations are widely used in static and high-throughput sensing applications such as security screening and industrial inspection. However, in ultra-near-field operation regimes, deviations from the PCA become more pronounced, particularly when the target range is comparable to array dimensions. Under such conditions, unmodeled bistatic effects may introduce phase and localization errors that degrade imaging accuracy.

In addition, practical MIMO implementations are sensitive to inter-channel mismatches arising from manufacturing tolerances, mutual coupling, and timing synchronization errors. These factors can disrupt phase coherence, which is critical for accurate wavenumber-domain reconstruction. Consequently, robust calibration strategies, including self-calibration methods and data-driven autofocus techniques using known reference targets, remain important areas of ongoing research.

7.4. Wave Propagation Modeling in Heterogeneous and Dispersive Media

Most frequency-domain reconstruction methods assume homogeneous propagation media with constant wave velocity. However, many practical applications, particularly biomedical imaging and NDT, involve heterogeneous and lossy materials with spatially varying dielectric properties.

In such environments, wave propagation is influenced by refraction, attenuation, and dispersion effects, which can be described using a frequency-dependent complex wavenumber formulation. Spatial variations in permittivity may introduce phase distortions that manifest as defocusing, depth misalignment, or target masking in reconstructed images.

To mitigate these effects, improved forward models that incorporate spatially varying media properties are being investigated. In particular, extensions of diffraction tomography and multi-layer propagation models, as well as modified wavenumber migration techniques capable of accommodating non-uniform dielectric distributions, are of interest as computationally efficient alternatives to full-wave numerical solvers.

8. Conclusions

This paper has reviewed the principal imaging algorithms for mm-wave FMCW near-field systems, covering six categories of techniques from the straightforward DAS beamformer to CS and sparse recovery. A central finding, confirmed repeatedly across the reviewed literature, is that the near-field spherical propagation model is not a theoretical nicety but a practical necessity: algorithms that substitute the planar-wave approximation

for the exact dispersion relation in (11) suffer measurable defocusing and localization errors at standoffs below 10 cm, errors that are unacceptable in NDT and medical applications where sub-millimeter accuracy is the design target. Among the spatial-domain methods, BPA with motion compensation stands out as the most robust choice for irregular scanning geometries, whether from a handheld wand or a moving vehicle platform, because it absorbs arbitrary aperture deviations directly into the per-voxel range computation without any additional correction stage.

Fast-BPA brings its cost in line with frequency-domain methods at $O\left(N^3 \log N\right)$, largely removing the historical argument against BPA on computational grounds. The planar $\omega - k$/RMA pipeline remains the workhorse for portal and raster-scan configurations, offering the best balance of speed and image quality when the aperture is well-controlled, while MIMO-RMA extends that efficiency to sparse physical arrays, which is increasingly relevant as system designers push for faster throughput without multiplying mechanical components. Compressed sensing occupies a narrower but genuinely useful niche in NDT and security scenarios where the scene really is sparse. NIHT and ℓ_1-minimization can recover high-quality images from 40% or less of the Nyquist samples, effectively trading computation time for scan time.

Looking ahead, three directions stand out as particularly worth pursuing. First, real-time GPU implementations of BPA remain an open engineering problem; the per-voxel parallelism of BPA maps naturally onto GPU architectures and closing the gap with the ω-k algorithm in wall-clock time would make it a practical option for live security screening. Second, learned priors for sparse recovery could relax the strict sparsity assumption that currently limits compressed sensing to isolated point-like scatterers, extending its applicability to more distributed target geometries. Third, reliable dielectric-corrected propagation models for medical imaging at heterogeneous tissue interfaces require further development; while current effective-wavenumber substitutions are useful approximations, they lose fidelity for targets deep within complex biological media. In summary, the gap between theoretical diffraction limits and real-world deployment is narrowing, with the remaining obstacles shifting from fundamental physical barriers to advanced engineering and computational optimization.

Author Contributions: Conceptualization, R.K.A. and D.T.; methodology, R.K.A. and D.T.; investigation, R.K.A. and D.T.; resources, R.K.A. and D.T.; data curation, R.K.A. and D.T.; writing—original draft preparation, D.T.; writing—review and editing, R.K.A.; supervision, R.K.A.; project administration, R.K.A.; funding acquisition, R.K.A. All authors have read and agreed to the published version of the manuscript.

Funding: This research received no external funding.

Data Availability Statement: No new data was created for this review article.

Conflicts of Interest: The authors declare no conflict of interest.

References

1. Vivet, D.; Checchin, P.; Chapuis, R. Localization and Mapping Using Only a Rotating FMCW Radar Sensor. *Sensors* **2013**, *13*, 4527–4552. [CrossRef] [PubMed]
2. Lee, J.; Li, Y.-A.; Hung, M.-H.; Huang, S.-J. A Fully-Integrated 77-GHz FMCW Radar Transceiver in 65-nm CMOS Technology. *IEEE J. Solid-State Circuits* **2010**, *45*, 2746–2756. [CrossRef]
3. Ramasubramanian, K.; Instruments, T. Using a complex-baseband architecture in FMCW radar systems. *Tex. Instrum.* **2017**, *19*, 1–10. [CrossRef]
4. Folster, F.; Rohling, H.; Lubbert, U. An automotive radar network based on 77 GHz FMCW sensors. In Proceedings of the IEEE International Radar Conference 2005, Arlington, VA, USA, 9–12 May 2005; pp. 871–876. [CrossRef]

5. Tessmann, A.; Kudszus, S.; Feltgen, T.; Riessle, M.; Sklarczyk, C.; Haydl, W.H. Compact single-chip W-band FMCW radar modules for commercial high-resolution sensor applications. *IEEE Trans. Microw. Theory Tech.* **2002**, *50*, 2995–3001. [CrossRef]
6. Zhang, Z.; Tian, Z.; Zhou, M. Latern: Dynamic Continuous Hand Gesture Recognition Using FMCW Radar Sensor. *IEEE Sens. J.* **2018**, *18*, 3278–3289. [CrossRef]
7. Li, C.; Chen, W.; Liu, G.; Yan, R.; Xu, H.; Qi, Y. A Noncontact FMCW Radar Sensor for Displacement Measurement in Structural Health Monitoring. *Sensors* **2015**, *15*, 7412–7433. [CrossRef] [PubMed]
8. Scherr, S.; Afroz, R.; Ayhan, S.; Thomas, S.; Jaeschke, T.; Marahrens, S.; Bhutani, A.; Pauli, M.; Pohl, N.; Zwick, T. Influence of Radar Targets on the Accuracy of FMCW Radar Distance Measurements. *IEEE Trans. Microw. Theory Tech.* **2017**, *65*, 3640–3647. [CrossRef]
9. Molaei, A.M.; Hu, S.; Fusco, V.; Fromenteze, T.; Kumar, R.; Albbasi, M.A.B.; Yurduseven, O. Advanced Near-Field Radar Imaging Approaches in Security: An overview on signal processing challenges, opportunities, and future directions. *IEEE Signal Process. Mag.* **2025**, *42*, 126–146. [CrossRef]
10. Liu, J.; Zhang, K.; Sun, Z.; Wu, Q.; He, W.; Wang, H. Concealed Object Detection and Recognition System Based on Millimeter Wave FMCW Radar. *Appl. Sci.* **2021**, *11*, 8926. [CrossRef]
11. Yang, J.; Thompson, J.; Huang, X.; Jin, T.; Zhou, Z. FMCW radar near field three-dimensional imaging. In Proceedings of the 2012 IEEE International Conference on Communications (ICC), Ottawa, ON, Canada, 10–15 June 2012; pp. 6353–6356. [CrossRef]
12. Bui, Q.C.; Lin, W.; Huang, Q.; Byun, G.-S. Automated Internal Defect Identification and Localization Based on a Near-Field SAR Millimeter-Wave Imaging System. *IEEE Access* **2025**, *13*, 24698–24716. [CrossRef]
13. Yalcinkaya, B.; Aydin, E.; Kara, A. Millimeter-Wave SAR Imaging for Sub-Millimeter Defect Detection with Non-Destructive Testing. *Electronics* **2025**, *14*, 689. [CrossRef]
14. Maier, M.; Paul, S.; Rother, M.; Di Meo, S.; Pasian, M.; Schoebel, J.; Issakov, V. Microwave Imaging for Breast Cancer Detection—A Comparison Between VNA and FMCW Radar. *IEEE J. Microw.* **2025**, *5*, 291–304. [CrossRef]
15. Li, X.; Bond, E.J.; Van Veen, B.D.; Hagness, S.C. An overview of ultra-wideband microwave imaging via space-time beamforming for early-stage breast-cancer detection. *IEEE Antennas Propag. Mag.* **2005**, *47*, 19–34. [CrossRef]
16. Amineh, R.K. Developments in Three-Dimensional Near-Field Imaging with FMCW Radar: A Comparative Study. *AIMS Electron. Electr. Eng.* **2020**, *4*, 359–368. [CrossRef]
17. Xu, Z.; Liu, X. Near-Field FMCW SAR Imaging with Fast BPA. In Proceedings of the ICASSP 2025—IEEE International Conference on Acoustics, Speech and Signal Processing, Hyderabad, India, 6–11 April 2025; pp. 1–5.
18. Haegelen, M.; Briese, G.; Essen, H.; Tessmann, A. Millimetre Wave Near Field SAR Scanner for Concealed Weapon Detection. In Proceedings of the European Conference on Synthetic Aperture Radar (EUSAR), Friedrichshafen, Germany, 2–5 June 2008; pp. 1–4.
19. Schorlemer, J.; Schulz, C.; Pohl, N.; Rolfes, I.; Barowski, J. Compensation of Sensor Movements in Short-Range FMCW Synthetic Aperture Radar Algorithms. *IEEE Trans. Microw. Theory Tech.* **2021**, *69*, 5145–5159. [CrossRef]
20. Case, J.T.; Ghasr, M.T.; Zoughi, R. Nonuniform Manual Scanning for Rapid Microwave Nondestructive Evaluation Imaging. *IEEE Trans. Instrum. Meas.* **2013**, *62*, 1250–1258. [CrossRef]
21. Yanik, M.E.; Torlak, M. Near-Field MIMO-SAR Millimeter-Wave Imaging with Sparsely Sampled Aperture Data. *IEEE Access* **2019**, *7*, 31801–31819. [CrossRef]
22. Smith, J.W.; Torlak, M. Efficient 3-D near-field MIMO-SAR imaging for irregular scanning geometries. *IEEE Access* **2022**, *10*, 10283–10294. [CrossRef]
23. Muppala, A.V.; Nashashibi, A.Y.; Afshari, E.; Sarabandi, K. Fast-Fourier Time-Domain SAR Reconstruction for Millimeter-Wave FMCW 3-D Imaging. *IEEE Trans. Microw. Theory Techn.* **2024**, *72*, 7028–7038. [CrossRef]
24. Meng, Y.; Lin, C.; Zang, J.; Qing, A.; Nikolova, N.K. General Theory of Holographic Inversion with Linear Frequency Modulation Radar and its Application to Whole-Body Security Scanning. *IEEE Trans. Microw. Theory Techn.* **2020**, *68*, 4694–4705. [CrossRef]
25. Lopes, H.V.; Godinho, D.M.; Conceição, R.C. Quantitative Evaluation of Repeatability in Medical Microwave Imaging: A Systematic Review. *IEEE Access* **2025**, *13*, 202524–202538. [CrossRef]
26. Xue, Z.; Li, L.; Nan, Y.; Zou, F.; Xu, Z.; Yang, T.; Wang, R. A Sinogram Decimation Fast Back-Projection Algorithm for Strip-Map SAR Imaging. *IEEE J. Sel. Top. Appl. Earth Obs. Remote Sens.* **2025**, *18*, 6790–6805. [CrossRef]
27. Li, C.; Peng, Z.; Huang, T.-Y.; Fan, T.; Wang, F.-K.; Horng, T.-S.; Munoz-Ferreras, J.-M.; Gomez-Garcia, R.; Ran, L.; Lin, J. A Review on Recent Progress of Portable Short-Range Noncontact Microwave Radar Systems. *IEEE Trans. Microw. Theory Tech.* **2017**, *65*, 1692–1706. [CrossRef]
28. Song, S.; Lu, J.; Xing, S.; Quan, S.; Wang, J.; Li, Y.; Lian, J. Near Field 3-D Millimeter-Wave SAR Image Enhancement and Detection with Application of Antenna Pattern Compensation. *Sensors* **2022**, *22*, 4509. [CrossRef] [PubMed]
29. Zhuge, X.; Yarovoy, A.G. Three-Dimensional Near-Field MIMO Array Imaging Using Range Migration Techniques. *IEEE Trans. Image Process.* **2012**, *21*, 3026–3033. [CrossRef] [PubMed]

30. Sheen, D.M.; McMakin, D.L.; Hall, T.E. Three-dimensional millimeter-wave imaging for concealed weapon detection. *IEEE Trans. Microw. Theory Tech.* **2001**, *49*, 1581–1592. [CrossRef]
31. Hao, Z.; Wang, R.; Peng, J.; Dang, X. Static Hand Gesture Recognition Based on Millimeter-Wave Near-Field FMCW-SAR Imaging. *Electronics* **2023**, *12*, 4013. [CrossRef]
32. Zhang, H.; Zong, H.; Qiu, J. Research on a Near-Field Millimeter Wave Imaging Algorithm and System Based on Multiple-Input Multiple-Output Sparse Sampling. *Photonics* **2024**, *11*, 698. [CrossRef] [PubMed]
33. Shao, W.; Hu, J.; Ji, Y.; Zhang, W.; Fang, G. W-Band FMCW MIMO System for 3-D Imaging Based on Sparse Array. *Electronics* **2024**, *13*, 369. [CrossRef]
34. Wang, S.; Li, S.; An, Q.; Bi, Z.; Zhao, G. Efficient range migration algorithm for near-field MIMO array imaging. *Digit. Signal Process.* **2023**, *133*, 103835. [CrossRef]
35. Gezimati, M.; Singh, G. Curved Synthetic Aperture Radar for Near-Field Terahertz Imaging. *IEEE Photon. J.* **2023**, *15*, 5900113. [CrossRef]
36. Reissland, T.; Lurz, F.; Weigel, R.; Koelpin, A. Compressed Sensing Based Near-Field Radar Target Imaging and Localization Employing Normalized Iterative Hard Thresholding. In Proceedings of the IEEE Topical Conference on Wireless Sensors and Sensor Networks (WiSNet), Orlando, FL, USA, 20–23 January 2019; pp. 1–3.
37. Álvarez-Narciandi, G.; López-Portugués, M.; Las-Heras, F.; Laviada, J. Freehand, Agile, and High-Resolution Imaging with Compact mm-Wave Radar. *IEEE Access* **2019**, *7*, 95516–95526. [CrossRef]
38. Yanik, M.; Torlak, M. Near-Field 2-D SAR Imaging by Millimeter-Wave Radar for Concealed Item Detection. In *2019 IEEE Radio and Wireless Symposium (RWS)*; IEEE: New York, NY, USA, 2019; pp. 1–4. [CrossRef]
39. Zhang, X.; Chang, T.; Wang, Z.; Cui, H.-L. Three-Dimensional Terahertz Continuous Wave Imaging Radar for Nondestructive Testing. *IEEE Access* **2020**, *8*, 144259–144276. [CrossRef]
40. Qian, J.; Zhou, J.; Ding, Z.; Liu, L.; Yang, X.; Wang, Q. Nondestructive Testing Based on Near Field THz SAR Imaging. In Proceedings of the 2023 24th International Vacuum Electronics Conference (IVEC), Chengdu, China, 25–28 April 2023; pp. 1–2. [CrossRef]
41. Singh, A.; Kumar, P.; Chakravarty, T.; Singh, G.; Bhooshan, S. A Novel Digital Beamformer with Low Angle Resolution for Vehicle Tracking Radar. *Prog. Electromagn. Res.* **2006**, *66*, 229–237. [CrossRef]
42. Hai, Y.; Zhang, L.; Shao, Z.; Li, Z.; Yang, B.; Pu, W.; Aln, H.; Wu, J.; Yang, J. Design and Implementation of a Near-Field Ultrahigh-Resolution Millimeter-Wave Radar Scanning 3-D Imaging System. *IEEE Trans. Aerosp. Electron. Syst.* **2025**, *61*, 14687–14702. [CrossRef]
43. Peng, J.; Kai, L.; Zheng, X.; Gao, J. Research and Implementation of Mm-Wave SAR Near-Field Imaging System. In Proceedings of the 2024 5th International Symposium on Computer Engineering and Intelligent Communications (ISCEIC), Wuhan, China, 8–10 November 2024; pp. 21–26. [CrossRef]
44. Pardhasaradhi, S.; Srihari, P. SAR Imaging with Automotive Radar: Range Migration Algorithm, Experiment, and Future Directions in Automotive Vehicle. In Proceedings of the 2022 IEEE 7th International Conference on Recent Advances and Innovations in Engineering (ICRAIE), Mangalore, India, 1–3 December 2022; pp. 382–387. [CrossRef]

Disclaimer/Publisher's Note: The statements, opinions and data contained in all publications are solely those of the individual author(s) and contributor(s) and not of MDPI and/or the editor(s). MDPI and/or the editor(s) disclaim responsibility for any injury to people or property resulting from any ideas, methods, instructions or products referred to in the content.